A 27-Al NMR study of the structure of lanthanum and yttrium based alumino–silicate glasses and melts

P. Florian, N. Sadiki, D. Massiot, J.P. Coutures

A ^{27}Al NMR study of the structure of lanthanum and yttrium based aluminosilicate glasses and melts

P. Florian[a*1], N. Sadiki[b], D. Massiot[a] and J.P. Coutures[b]

[a] CRMHT, CNRS UPR 4212, FR2950, 1D av. Recherche Scientifique 45071 Orléans Cedex 2, France
[b] PROMES, Rambla de la Thermondynamique, Tecnosud, 66100 Perpignan, France

Abstract

We have investigated by ^{27}Al Nuclear Magnetic Resonance spectroscopy some compositions in the Ln_2O_3–Al_2O_3–SiO_2 (Ln=Y or La) ternary phase diagram containing more than 60 mol% of SiO_2. One– and two–dimensional high–field (17.6 T) high–speed (30 kHz) Magic Angle Spinning experiments have been performed along with simulations of the spectra to quantify the amount of penta–coordinated aluminum present in those glasses as a function of composition. Very high–temperature experiments have allowed to follow selected samples from 2200°C down to 1700°C and hence to characterize the aluminum coordination state and dynamics in those liquids.

The present study re–enforces the current view that "minor" species such as penta–coordinated aluminum are actually present in considerable amount in aluminosilicate glasses and high–temperature liquids at and above the charge compensation join. The high–field strength of Y^{3+} and La^{3+} reveal, for the first time in glasses, different mean electric field gradient perceived by the tetra– and penta–coordinated aluminum environments. The movements responsible for the NMR relaxation of aluminum in the high–temperature liquid are showed to be uncorrelated with the movements responsible for the macroscopic shear viscosity. Results obtained both on glasses and *in–situ* at high–temperature suggest a preferential localization of Ln^{3+} nearby tetra–coordinated aluminum species, with possible formation of tricluster and/or Ln^{3+} coordination changes.

[1] corresponding author

Introduction

Rare earth aluminosilicate glasses have attracted large attention from the material sciences community due to their interesting physical and chemical properties like high glass-transition temperature[1-4] (T_g ~ 900°C); attractive mechanical properties such as high hardness (~ 8 GPa) and elastic modulus (~ 100 GPa)[5-9] or great chemical durability (normalized losses at high surface-volume S/V ratio of Si, Al and Ln ~ $10^{-5\ to}$ 10^{-7} g/m^{2}j).[10-14] Therefore this family of glasses has a large range of applications in modern technology like (a) host materials for laser, optical storage or optical communication; (b) bonding agent for silicon nitride ceramics; (c) matrix for the storage of long-lived actinides. These glasses, with or without small amounts of alkali modifiers, can be also considered as model systems for the study of potential matrix for the storage of long lived actinides (Pu as well as minor actinides). Yttrium and lanthanum has been chosen to simulate actinides because firstly their Ln_2O_3–Al_2O_3–SiO_2 phase diagrams as well as relevant physico-chemical properties are known, and secondly spectroscopic studies with multinuclear (^{27}Al and ^{17}O) NMR can be carried out to obtain structural information without the problems of paramagnetism observed with other rare earth cations.

Studies of the phase diagram have been carried out on the La_2O_3–Al_2O_3–SiO_2 and Y_2O_3–Al_2O_3–SiO_2 systems (further denoted LAS and YAS respectively) at 1300°C in air[15] and up to 1700°C under nitrogen.[16] The phase relationships in the systems Ln_2O_3-Al_2O_3-SiO_2 have also been reported[17] and recently a thermodynamical assessment of the Y_2O_3-Al_2O_3-SiO_2 system[18] has been found to be in good agreement with previous experimental works.[19,20] The thermo–chemical behavior of those rare-earth aluminosilicate has been explored using DTA[4,21] and calorimetric studies[22,23] and their crystallization behaviors have been assessed.[21]

The structure of LAS and/or YAS glasses have been investigated by ultrasonic measurements[24], Raman[3] and FTIR[3,4,28,30] spectroscopies and solid–state NMR[25-30] spectroscopy (standard magnetic fields) over the last decade. It has been suggested that rare earth aluminosilicate glasses lack structure beyond the short range and that a wide distribution of types of non-bridging oxygen ions exists for these glasses.[3] The general disorder in the silicate network is due to a wide distribution of Q_n units with the presence of Q_2 but also more polymerized Q_3 and Q_4 units,[4]. Density and fractal bond connectivity models suggest a two-dimensional layer structure.[24] The rare earth act as a modifier except at high lanthanum content (> 25 mol%) where the formation of co–ordinate links prevails on the reduction of cross links.[4] Previous ^{27}Al NMR studies, carried out at moderate principal fields and spinning rates,

show that the dominant aluminum species is AlO_4 in conjunction with the existence of small amounts of AlO_5 and/or AlO_6. Nevertheless the strong overlap of the various ^{27}Al MAS NMR lines obtained for those glasses preclude quantification and only semi-qualitative evolutions have been derived from the spectra analysis.

The goal of this study is therefore to improve the characterization of the aluminum environments in La– and Y– aluminosilicate glasses using a combination of high magnetic field and high spinning speed which have been available only recently. ^{27}Al NMR experiments were also performed *in situ* in the high–temperature molten state in order to characterize the temperature dependence of their structure and dynamics.

Experimental

All samples were synthesized from the commercially available oxides La_2O_3 (99.0%, Prolabo), Y_2O_3 (99.4%, Prolabo), Al_2O_3 (99.9%, Pechiney) and SiO_2 (99.5% Prolabo). La_2O_3 was first pre-heated in an alumina crucible during two hours at 1100°C to remove anionic impurities, mixed with the other component and heat-treated a second time. Yttria based samples were not subjected to heat treatments since they are well known to be free of such impurities. The mixtures were then melted at around 2000°C under air during approx. 2 mn on a water-cooled aluminum plate associated to a vertical axis laboratory scale solar furnace of 2 kW with an average solar flux of 900 to 1000 W/m^2. The temperature and melting time were chosen to ensure a good chemical homogeneity of the glasses as well as to prevent any compositional shifts due to the preferential vaporization of silica. Upon suddenly removing the samples from the solar furnace's focus point the samples were cooled at a cooling rate of ~200°C/s and transparent quasi-spherical glassy droplets of 2 to 6 mm diameter were obtained. The glass compositions were analyzed by SEM-EDX analysis (SEM: Hitachi S 4500, EDS: Kevex) after gold metallization and using a beam energy of 15 keV. Glass transition and crystallization temperatures were previously determined by differential thermal analysis performed on small glass pieces.[21] In table 1 we report the glasses compositions and the thermal events observed: namely T_g (glass transition temperature), T_c (first observed crystallization thermal event) and T_m (melting temperature) when the melting of the crystallized glass is observed (see reference 21 for details). Figure 1 gives the position of each composition on the ternary Ln_2O_3-Al_2O_3-SiO_2 system.

All NMR room–temperature experiments were performed on a 17.6 T Bruker Avance 750 spectrometer operating at 195.47 MHz and equipped with a 2.5 mm MAS probe. For all experiments, chemical shifts were externally referenced to 1M aqueous $Al(NO_3)_3$.

1D single pulse experiments were performed while spinning the sample at 30 kHz, with a short (1 μs = π/20) pulse using a 25 kHz radio-frequency field, 8000 scans and a spectral width of 2 MHz allowing the acquisition of the extended set of spinning sidebands. The removal of the rolling baseline due to dead time truncation was done afterwards using a manually defined spline function. ^{27}Al spin-lattice relaxation times T_1 were estimated to be 1.5 s (sample Y04A21) and 5.5 s (sample L02A23) and the recycle delay was then set to 0.5 s for all compositions to allow for a full relaxation of the spin system after the small tip angle pulse used.

2D triple-quantum MAS experiments were obtained using a shifted-echo[31] sequence with a 30.03 kHz spinning speed. An rf–field strength ν_{rf} = 150 kHz was used leading to optimal excitation and reconversion pulse of 3.0 and 1.1 μs respectively whereas the 20 μs π refocusing pulse was performed at ν_{rf} = 7 kHz. ^{27}Al spin-spin relaxation times T_2 were estimated to be 30 ms (sample Y04A21) and 25 ms (sample L02A23) and the echo shift was set to 50 rotor periods (i.e. 1.65 ms). The recycle delay was 0.3 s, 480 scans were accumulated for each of the 16 t_1 slices with an increment of 33.3 μs (i.e. a rotor-synchronized acquisition in the t_1 dimension[32]).

All high–temperature experiments were performed on a 7.04 T Bruker Avance 300 spectrometer operating at 78.2 MHz and equipped with a previously described laser-heated home-built setup and time resolved acquisition conditions.[33,34] The sample weighting between 50 and 150 mg is placed in a convergent-divergent boron nitride nozzle allowing levitation on an air jet while heated from the top and the bottom by two computer-controlled CO_2 lasers. This allows the observation of the liquid phase and the recording of NMR spectra during the cooling of the sample at a rate of approx. 200°C/s after switching off the lasers. The applied pulse width was 40 μs (π/2 pulse), the spectral width 10 kHz and the recycle delay 50 ms. Chemical shift are given with reference to a 1 M $Al(NO_3)_3$ solution at room temperature and hence uncertainty is approx. ± 0.5 ppm. The temperature of the sample is measured with an optical pyrometer (λ = 0.85 nm) through a fiber whose end is placed 75 mm above the sample inside the magnet. A temperature calibration is performed by cooling samples of Al_2O_3 with various weights and recording their well marked temperature plateau due to crystallization at 2054 C. Since the compositions studied here contain a high proportion SiO_2 known to easily vaporize, only two cooling experiments were performed with each sample using a starting temperature as low as possible. With those precautions the total heating time for each sample was less than 20 s and the weight loss were kept between 2 and 7%.

Results

Figure 2 shows a stack plot of the ^{27}Al MAS one-pulse spectra obtained for all the samples. Apart from the spinning sidebands of the external <±3/2,±1/2> transitions visible on the sides of the main peak, the central <-1/2,1/2> transition appears as an asymmetric peak typical of aluminate and aluminosilicate glasses. Those sharp left edge lineshapes which can clearly be seen from the La30A15 composition are characteristic of a wide distribution of quadrupolar coupling constants C_Q combined with a distribution of isotropic chemical shift.[35] A main peak is seen around 50 ppm (position of the maximum) but a second shoulder around 30 ppm and a bump around 0 ppm visible for some compositions evidence the presence of two other spectral components. The three peaks are classically assigned to four- five- and six-fold coordinated aluminum environments (Al_{IV}, Al_V and Al_{VI} respectively) and are clearly distinguished by the MQMAS experiments as seen in figure 3.

As seen from the comparison with the 9.4 T spectra (figure 3) the use of high 17.6 T principal magnetic field does resolve better those components with respect to the previous studies performed at 9.39 T[25,26,28,30] or 11.7[27,29] and 14.1 T.[27] Nevertheless these spectra still do not provide lines separation which indicates the presence of a large average value of the quadrupolar coupling constant. The combined use of higher field and higher spinning speed (30 kHz) efficiently simplifies the spectra by removing the spinning sidebands from the central part of the spectrum. Previously observed trends[26,30] are confirmed upon direct inspection of those spectra: the positions of the peaks do not vary much with composition, the proportion of Al_V and Al_{VI} increases upon decreasing the rare-earth content, the peaks of the YAS glasses are broader than their LAS counterparts. There is also an already mentioned tendency for the YAS glasses to contain more Al_V species than their equivalent LAS composition.

Considering the fact that the MQMAS experiment is intrinsically not quantitative and because of the strongly overlapping nature of the 1D peaks, it is necessary to perform a careful simulation of the one-pulse experiments to extract the population of the three aluminum species. The distribution of C_Q can be handled by using the approach originally developed by Czjzek *et al.*[36] further formulated into a general model for the distribution of electric field gradients in disordered solids by Le Caër *et al.*[37] and implemented along with a distribution of isotropic chemical shift in our laboratory developed simulation software DmFit.[35,38] Each component is then described by a set of four independent parameters: amplitude, mean isotropic chemical shift $\overline{\delta}_{iso}$, width $\sigma(\delta_{iso})$ of the distribution of δ_{iso} and a mean quadrupolar coupling constant $\overline{C}_Q$. In order to get the most reliable trends of intensities from the 1D ex-

periments, $\overline{C}_Q$ and $\sigma(\delta_{iso})$ for the small Al_V and Al_{VI} components were fixed to 8.5 MHz and 15.0 ppm respectively, those values being obtained from simulations (all parameters optimized) of the spectra presenting the biggest amount of those two species. Those parameters were optimized for the simulations of the MQMAS experiments except for the Al_{VI} sites which are invisible in almost all 2D spectra and hence not reported in table 2 for clarity reasons. Finally, the spinning sidebands manifold arising from the external <±3/2,±1/2> transitions were also taken into account and calculated using the quadupolar and chemical shift parameters obtained from the central transition. An example of the resulting 1D and 2D simulations can be found in figure 3 and the list of all fitted parameters is given in table 2.

The simulations of the 1D experiments not only accounts closely for the shapes of the central transition but also for the positions and intensity of the spinning sidebands relevant to the outer transitions. The more challenging simulations of the 2D results do reproduce most of the observed spectra except for the higher coupling region which is known to be truncated by the 3Q excitation. The main parameter influenced by the composition is clearly the population of the various species which varies over a range of 20% for YAS and LAS glasses. The isotropic chemical shift of the Al_{IV} species is found to be weakly linked to composition, being 64.5 ppm ± 1 ppm for the YAS glasses and 63.0 ppm ± 1 ppm for the LAS compositions, in good agreement with previous published values.[26] Mean isotropic chemical shifts obtained for the Al_V species are 34.8 ppm ± 1 ppm for the YAS compositions and 35.8 ppm ± 1 ppm for the LAS one whereas the values obtained for the Al_{VI} species lie typically in the range 9 – 12 ppm ± 2 ppm but are significantly scattered due to the very small amount of Al_{VI} found in most compositions. For all compositions, $\overline{C}_Q^{IV}$ is found between 9 and 11 MHz which is higher than the values obtained by Schaller *et al*[26] from their MQMAS spectra by a factor of two. As seen from our own results, $\overline{C}_Q$ derived from the MQMAS experiments is systematically lower by ~ 1.5 MHz than the values obtained from the one-pulse experiments because of the well known lack of efficiency of the 3Q excitation and reconversion in the case of very strong quadrupolar couplings. Moreover, such aluminum sites experiencing strong electric field gradients (EFGs) will give rise to very wide lines which are difficult to observe at low magnetic field such that the combination of low field and MQMAS filters out part of the signal coming from highly distorted aluminum environments and hence explains the higher values measured in this study. A very surprising result is that $\overline{C}_Q^{IV}$ is found systematically bigger

than $\overline{C}_Q^V$, a behavior which has –to our best knowledge– never been observed before in aluminum containing glasses.

One of the most valuable information extracted from the simulations and which was absent from the previous studies on those systems are the evolution of the population of the various aluminum environments as a function of composition. This is reported in figure 4 for the two major Al_{IV} and Al_V species as a function of the molar ratio $[Al_2O_3]/[Ln_2O_3]$ and the molar SiO_2 content $[SiO_2]$. The above-mentioned qualitative trends are confirmed: the population of Al_V increases upon decreasing the rare-earth content and YAS glasses contain more Al_V than LAS ones. At fixed SiO_2 content, no clear distinction can be made between the Y– or La– containing glasses, but the Al_V population is still inversely proportional to the rare-earth content. It is also seen that the Al_V population decreases with increasing $[SiO_2]$.

The high–temperature spectra consist in a single Gaussian/Lorentzian line (figure 5) from which a position δ and a full width at half maximum $\Delta\nu_{1/2}$ can be extracted. As previously observed,[39] the presence of SiO_2 increases the linewidth with respect to aluminates[33,34,40] and the signal–to–noise ratio of those one–scan spectra is therefore low for small samples and at "low" temperature. Taking into account the weight losses, the difficulty to reproduce precisely the same experimental setup, and since $\Delta\nu_{1/2}$ varies from 350 to 1500 Hz, one can assume that the uncertainty on the absolute value of δ ranges from ± 0.5 ppm to ± 2 ppm upon reaching the highest $\Delta\nu_{1/2}$ values. The temperature evolution obtained during the cooling of a sample is on the other hand fully reliable since it is performed during a period of time short enough (2 s) to prevent any variations in the experimental setup. A series of acquisitions at constant temperature around 2000°C is done during 0.5 s before switching off the lasers, giving a set of data representative of the effect of composition and listed in table 3.

The evolution of the positions during the cooling and hence as a function of the temperature are plotted in figure 6 where only the values obtained at the highest temperature are used since the linewidth increases very quickly as the temperature drops. The high temperature chemical shifts evolve linearly with temperature with slopes $\Delta\delta/\Delta T$ (table 3) in the range -3 to 3 ppm/1000°C, to be compared to the value of 5.2 ppm/1000°C obtained here for Al_2O_3 or -6.0 ppm/1000°C for $CaAl_2O_4$.[34] The higher value of $\Delta\delta/\Delta T$ found for Al_2O_3 with respect to the 2.5 ppm/1000°C obtained previously[33] is very probably due to a different experimental procedure (bigger sample and lower starting temperature were used here) and the tendency of alumina to produce non–stoichiometric melts.[41] For all measurements displayed here the uncertainty is nevertheless only ± 1 ppm/1000°C since they have been performed within the

same experimental conditions and the compositions do not present oxygen non–stoichiometry. Within this uncertainty, there is a linear increase of $\Delta\delta/\Delta T$ with increasing concentration of $[Ln_2O_3]$ as seen in figure 7. We also plotted in figure 6 the average isotropic chemical shift extrapolated from the sum of the positions of the various Al_{IV}, Al_V and Al_{VI} components found in the MAS spectra weighted by their respective population. If the extrapolated position at T_g does not meet this solid–state weighted average as for $CaAl_2O_4$, it nevertheless falls within a few ppm from this value (keeping in mind the difficulties in measuring very precise positions in the liquid at rather "low" temperature). In order to extract the dependence of the high–temperature line position with the composition, we plotted in figure 7 the value of the position obtained at 1900°C from the linear fit displayed in figure 6 (given as $\delta_{1900°C}$ in table 3). This shows that the position decreases with increasing $[Al_2O_3]/[Ln_2O_3]$ ratio and is systematically higher for LAS than for YAS. Evolution of those trends upon changing the temperature lies nevertheless within the uncertainty of our measurements and can not therefore be evidenced here.

For the YAS compositions between 2100°C down to 1500°C $\Delta\nu_{1/2}$ is found in the range 450 to 1500 Hz whereas this range reduces to 300 to 950 Hz for the LAS samples (table 3). This is to be compared with Al_2O_3: 80 – 250 Hz, $CaAl_2O_4$: ~ 120 Hz[34], strontium aluminates: ~ 100 Hz[40], calcium aluminosilicate ($SiO_2 \leq 44$ mol%): 300 – 550 Hz[39,42] and the binary Al_2O_3-SiO_2 system : 100 – 800 Hz[43]. If we have reached at high temperature the fully average motional regime, $\Delta\nu_{1/2}$ is related to the spin-lattice relaxation time T_1 by the equation:

$$T_1 = \frac{1}{\pi\Delta\nu_{1/2}} \qquad (1)$$

This has been experimentally checked in the previous high–temperatures levitation experiments performed in our laboratory[33,34,39,40]. It could not be checked for the studied compositions because those measurements require holding the sample at elevated temperature during several minutes during which compositional drift (due to high silica content) occur. This relationship is nevertheless true for aluminosilicates containing up to 44 mol% SiO_2 [39] and we have no reasons to believe that equation 1 is not a good approximation in our case. Under the hypothesis that the dominant relaxation mechanism is driven by the fluctuation of the quadrupolar interaction with an exponential correlation function, T_1 can in turn be expressed according to[45] :

$$\frac{1}{T_1} = \frac{3}{10}\pi^2 \frac{2I+3}{I^2(2I-1)} \widetilde{C}_{Q\eta}^2 \tau_c^2 \qquad (2)$$

where τ_c is the correlation time of the fluctuation of the quadrupolar interaction, I is the nuclear spin (5/2 for ^{27}Al), and the time–averaged dynamic quadrupolar product[46] $\widetilde{C}_{Q\eta} = \widetilde{C}_Q \sqrt{1+\widetilde{\eta}_Q^2/3}$ of the aluminum sites. Assuming that the systems investigated here are ergodic and that the glassy state is a good approximation of a frozen liquid state, the time–averaged $\widetilde{C}_{Q\eta}$ can be statistically approximated by the spatially–averaged $\overline{C}_{Q\eta} \sim 10$ MHz (using $\overline{C}_Q$ measured at room temperature and $\overline{\eta}_Q = 0.6$ as in the GIM model) and equation 2 allows to derive τ_c from $\Delta\nu_{1/2}$. This set of equation has initially been developed within the framework of quadrupolar relaxation by molecular reorientation in liquids[45] using the classical BPP model[47] or in other words "Brownian motion in a liquid or non–crystalline solid"[47]. If the quadrupolar interaction is certainly the dominant interaction contributing to the relaxation, a molecular reorientation takes only into account the thermal vibration mechanism and not the bond breaking one expected in such high–temperature liquids. Although rather simplistic, this approach has proven in the past to be a successful approximation of the dynamics observed in molten aluminates and aluminosilicates by ^{27}Al NMR[33,34,39,40,42,43].

The logarithm of τ_c derived from the NMR linewidth is plotted against 1000/T in figure 8 for all compositions investigated here. Within the uncertainty of our measurement there is no marked difference in τ_c neither by varying the composition for a given type of lanthanide nor between YAS and LAS compositions for which around 2000°C (1000/T ~ 0.57) $\tau_c \sim 18.0 \pm 6$ ps and 12.7 ± 6 ps respectively (see table 3 for details). The effect of composition is therefore probably small and masked by the uncertainty related to the measurement of the linewidth as well as the small compositional drift experienced by the samples upon heating. On the other hand, the values of 3.7 ps found for supercooled Al_2O_3 around 2000°C is significantly smaller and is a consequence of the absence of SiO_2 in this melt. It can be noticed that those correlation times of a few pico–seconds are within the lower end of the acoustic vibrations time scale. Thermal vibrations and rotations of the local aluminum environment represent therefore the major contribution to the EFG fluctuations which leads to the NMR relaxation, in agreement with the type of motion used by the BPP model.

Since high-temperate viscosity measurements are available for some YAS compositions[48] it is interesting to compare the NMR correlation times with the relaxation time for viscous flow τ_η related to the viscosity η according to the Maxwell equation:

$$\tau_\eta = \frac{\eta}{G_\infty} \quad (3)$$

where $G_\infty = 10^{10\pm0.5}$ Pa is the shear modulus at infinite frequency which is known to depend little on both temperature and composition for aluminosilicate melts[49]. The resulting values are also displayed in figure 8 for compositions number 4, 5 and 6 of reference 48 containing the highest amount of SiO_2 and which would in our mol% notation transcribe as Y14A20, Y17A19 and Y20A18 respectively. There is a clear mismatch between the absolute value of τ_η and τ_c below 1900°C (keeping in mind the uncertainty on G_∞ as well as $\widetilde{C}_{Q\eta}$ both parameters introducing a constant offset in $\ln(\tau)$).

The effect of temperature is clearly monotonic, the temperature range explored is too limited to sample properly the expected[39] Tamman-Vogel-Fulcher equation and a linear behavior is observed. The slopes of the $\ln(\tau)=f(1000/T)$ are reliably different and the Arrhenius activation energies E_a can be measured from the curves plotted in figure 9 and are reported in table 3 together with literature data. YAS compositions show the lowest activation energies between 39.8 and 73.3 kJ/mol compared to the range of 55.4 to 129 kJ/mol found for LAS samples. For both systems E_a shows a tendency to decrease with increasing $[Al_2O_3]/[Ln_2O_3]$ molar ratio (as well as increasing $[Ln_2O_3]$ molar content). The activation energy for Al_2O_3 lies in between the values found for YAS and LAS compositions whereas $CaAl_2O_4$ is found higher at 142 kJ/mol and $CaAl_2Si_2O_8$ even more (187 kJ/mol).

Discussion

A general framework of our discussion can be found in the generally accepted structural model used for alkali aluminosilicate glasses which assumes that alkalis act as network modifiers. Its extension to rare earth aluminosilicate glasses would imply that a single Ln^{3+} act as a charge compensator of three neighboring $[Al_{IV}]^-$. It should nevertheless be noted that since the Al/Si ratio is less than 0.5 for all compositions studied here, a group of three neighboring aluminum atoms is statistically unlikely and the formation of highly coordinated species is not required to preclude two Al_{IV} species linked together (Lowenstein rule). This charge compensation can also be achieved by producing non-bridging oxygens either in $[Q_n]^{n-4}$ ($n < 4$) units or in Al_{IV} species, resulting in the depolymerization of the aluminosilicate glassy network. A bridging oxygen Si–O–Al is also susceptible to contribute in the charge compensation process, but bond valence consideration suggest that it should be bonded to no more than one Ln^{3+}. In a fully intermixed aluminosilicate glassy network where $(Si,Al)O_4$ tetrahedra are corner-sharing through bridging oxygens a combination of all the above mentioned species is

then expected to charge balance the addition of Ln^{3+} cations. Another effect of the addition of Ln_2O_3 is to stabilize the Al_{IV} species with respect to the Al_V and Al_{VI} units, the former being the dominant species in binary Al_2O_3-SiO_2 glasses.[50,51,29] Finally, another mechanism that has been proposed to stabilize Al_{IV} and favor non-bridging oxygens is the formation of tricluster[52] made of three tetrahedral species (either Si or Al) sharing a common oxygen, a species which has, up to now, been experimentally evidenced only in an aluminate glass.[54] Such minor species, along with the presence of non-bridging oxygens unexpectedly observed in fully polymerized compositions[53] are believed to be a key mechanism explaining the viscosity anomalies found in those liquids[52].

For a given $[Al_2O_3]/[Ln_2O_3]$ ratio, YAS compositions contain a significantly higher amount of Al_V species than the LAS ones (figure 4). Figure 3 shows also that Al_V species are formed at the expense of Al_{IV}, following the previously proposed[26] schematic reaction:

$$LnO_y + AlO_x \leftrightarrow LnO_{y-1} + AlO_{x+1} \quad \text{with } x = 4{,}5 \text{ and } y = 7{,}8 \qquad (4)$$

which is displaced to the right with increasing cation field strength. Using effective ionic radii[44] the field strength $3/r^2$ (in units of 10^5 pm^{-2}) for VI-, and VIII-fold coordination state of La^{3+} is 26.5 and 23.8, and for Y^{3+}: 30.6 and 27.3 respectively. The observed differences in Al_V populations between YAS and LAS systems are therefore in agreement with the field strength being bigger for yttrium than for lanthanum.

The biggest amount of Al_V is found as expected in the $[Al_2O_3]/[Ln_2O_3] > 3$ region where not enough Ln^{3+} is present to ensure the charge compensation of the Al_{IV} species. The presence of Al_V units is also evidenced at and below the $[Al_2O_3]/[Ln_2O_3] = 3$ charge compensation line (despite the fact that charge compensation should be reached) but this species quickly disappear upon decreasing the $[Al_2O_3]/[Ln_2O_3]$ ratio. The presence of high coordinated aluminum species in compositions without excess aluminum over charge-balancing cations has been previously observed in alkali[55], calcium[56,57] and magnesium[58] aluminosilicates glasses. In agreement with the lower field strength of Ca^{2+} (VI = 18.5) the proportion of Al_V is found here as high as 20%, i.e. above the range for calcium aluminosilicates[57] (up to 14%) for compositions with $[SiO_2] > 60$ mol%. The field strength of Mg^{2+} (IV = 30.3, VI = 25.0) is on the other hand on the order of the one of Y^{3+} and the small value of 6% found for Al_V in magnesium aluminosilicate[58] casts some doubts about the precision of those measurements, especially considering that preliminary results obtained in our laboratory give values as high as 50% (to be published). The small dependence upon composition of the Al_V amount in the peraluminous regions observed here is in contrast with the strong increase observed above the

tectosilicate join in the above mentioned calcium systems. This suggests the existence of another mechanism which stabilizes Al_{IV} species in this region and/or, according to equation 4, an increase of the Ln^{3+} coordination number reducing its ability to form Al_V by decreasing its field strength.

The rather high field strength of Ln^{3+} cations also induces strong distortions upon the average Al_{IV} environment leading to a $\overline{C}_Q^{IV}$ found here around 10 MHz, i.e. larger than the typical 6-7 MHz value found in calcium aluminosilicate glasses using the same lineshape simulation procedure.[57] Slightly larger isotropic chemical shift distributions $\sigma(\delta_{iso})$ are also observed in this study, consistent with more distributed aluminum environments. Due to the disordered nature of the samples, the EFG contribution of distant atoms is equivalent for all aluminum sites and the observed differences between $\overline{C}_Q^{IV}$ and $\overline{C}_Q^{V}$ has to come from local differences. Since high field strength cations seems to induce larger EFGs, the bigger $\overline{C}_Q^{IV}$ values can be seen as a consequence of the preferential location of Ln^{3+} nearby Al_{IV} units leading to species more distorted at a scale of a one to two bonds lengths.

The Al_{IV} mean isotropic chemical shift $\overline{\delta}_{iso}$ slightly decreases with increasing SiO_2 content going from approximately 65 ppm at 60 mol% SiO_2 to 62 ppm at 80 mol%. This small variation which is strictly speaking almost within the ± 1 ppm error bar, results from a decrease of the average number of Si atoms in the aluminum environment already observed previously[26] and particularly clearly evidenced in calcium-based glasses.[57]

This tendency is not clearly retrieved from the high–temperature experiments for which the line position seems to correlate better to the $[Al_2O_3]/[Ln_2O_3]$ molar ratio (figure 7). Since this averaged value δ is equal to $[Al_{IV}]\delta_{IV} + [Al_V]\delta_V + [Al_{VI}]\delta_{VI}$, it is a direct measure of the mean aluminum coordination number in the liquid–state. The higher values found for LAS compositions indicates therefore a lower concentration of Al_V in the La–containing melts than in their Y counterparts, consistent with our results obtained on glasses. As seen in figure 7, the lowest $\delta_{1900°C}$ position (i.e. highest concentration of Al_V) is found at high $[Al_2O_3]/[Ln_2O_3]$, a behavior also consistent with the room–temperature results. This decrease with increasing $[Al_2O_3]/[Ln_2O_3]$ is nevertheless small and here again the formation of important amount of Al_V in compositions close to pure binary aluminosilicates is countered by a mechanism stabilizing Al_{IV}. It should also be noticed that the high–temperature positions linearly extrapolated down to the glass–transition temperature T_g (figure 6) lie below the average solid–state value. This increase in δ at T_g shows that at some time in the cooling process part of the Al_V and

Al_{VI} species formed at high temperature are transformed back to Al_{IV} units. The aforementioned Al_{IV} stabilizing mechanism is therefore seemingly favored at low temperatures and in melts containing few modifiers, a behavior also expected for tricluster.[52]

The isostructural thermal evolution (i.e. pure thermal expansion, no changes in the aluminum speciation as a function of temperature) has been previously estimated from the Al_2O_3 behavior[34] and has been found around $\Delta\delta/\Delta T = 2.5$ ppm/1000°C. The sizable relative slope $(\Delta\delta/\Delta T)_{rel} = |\Delta\delta/\Delta T - 2.5|$ found here for the aluminosilicate compositions is then a clear indication of a structural thermal evolution, i.e. that Al_V species are favored at high temperature. $(\Delta\delta/\Delta T)_{rel}$ characterizes the behavior of the aluminum speciation as a function of temperature and hence the temperature dependence of the structure or, in other words, the "strong/fragile" character[59,60] of the liquid. The smaller $(\Delta\delta/\Delta T)_{rel}$ the "stronger" the liquid and hence finding the bigger $(\Delta\delta/\Delta T)_{rel}$ at low $[Al_2O_3]/[Ln_2O_3]$ content indicates that Ln_2O_3 increases the "fragile" character of the melts. Ln_2O_3 is here found to play a modifier role in the sense that it weakens the aluminosilicate network. Figure 7 shows also that for a given $[Al_2O_3]/[Ln_2O_3]$ content LAS liquids are slightly more "fragile" than the YAS melts.

It is also interesting to note that both $\delta_{1900°C}$ and $\Delta\delta/\Delta T$ but also the activation energy E_a (figure 9) seem to display, within the errors bars, a rather linear behavior as a function of $[Al_2O_3]/[Ln_2O_3]$. No changes can be seen at the charge compensation join, as opposed to the $[Al_V]$ variations described for the glasses. Since our study explores a temperature range between 2200°C and 1700°C, this strongly suggests that other mechanisms affecting the aluminum speciation are at play at lower temperature.

The oxygen self diffusivity D in silicate melts is known to be related to the shear viscosity η through the Eyring equation $D = kT/\eta\lambda$, k being the Boltzmann constant, T the temperature and λ the diffusive jump length. On the ground of the Eyring equation, one classically assumes in binary silicates that the Si–O bond breaking is the mechanism at the origin of the macroscopic shear viscosity of silicate melts.[49] Under this assumption the discrepancy between ^{27}Al NMR and viscosity measurements observed from correlation times (figure 8) as well as activation energies (figure 9) indicates that the movements responsible for the NMR relaxation of aluminum are not correlated with the oxygen diffusion. Since aluminum NMR relaxation probes here the thermal vibrations of the systems investigated those discrepancies are a clear sign of a decoupling between the bond breaking and the vibration time scales. The diffusion coefficient is schematically expressed as a function of the free enthalpy of motion

ΔH of the diffusing entity $D = D_0 \exp(-\Delta H/kT)$ and the preexponential factor $D_0 \propto \lambda^2 \tilde{\nu} \exp(-\Delta G_v/kT)$ contains the vibration frequency $\tilde{\nu}$, the jump distance λ and the free enthalpy ΔG_v of formation/motion of the defects allowing the diffusion. The diffusion and thermal vibrations are hence related but the oxygen jump triggered by $\tilde{\nu}$ happens in our case on a different time scale than the vibration $\tilde{\nu}$. These two time scales will couple in all liquids when the temperature is high enough since, as seen from the expression of D_0, the probability of a successful jump leading to diffusion depends upon temperature and viscosity. At $T/T_g \sim 2$ the coupling will occur only in most fragile liquids where viscosity is already very low and is therefore expected at low silica content. Such coupling is indeed seen in calcium aluminosilicate melts containing only 44 mol% of silica[39], molten alumina[33] or aluminates[34,40] and a decoupling is observed for strontium aluminosilicate melts[42] with more than 50 mol% of SiO_2.

The increase in correlation time τ_c going from pure Al_2O_3 to YAS and LAS reflects the slowing down of the EFG's fluctuations at the aluminum sites upon addition of SiO_2 (i.e. with an increase of the liquid's viscosity). This indicates that the aforementioned decoupling is not complete and that the spectral density of the movement driving the viscosity has also a non–zero component at the ^{27}Al Larmor frequency. If part of the ^{27}Al NMR relaxation is driven by the diffusion processes the most efficient mechanism remains the thermal vibrations. This is seen in figure 9 where the activation energies for YAS and LAS liquids are found very close to the one of Al_2O_3 which is dominated by vibrations since no changes in aluminum speciation is expected as a function of temperature (i.e. no contribution from oxygen diffusion). Higher activation energies found for $CaAl_2O_3$ and $CaAl_2Si_2O_6$ confirm the recoupling of the vibration and diffusion timescales in those two systems presenting significantly lower viscosities than YAS and LAS compositions studied here. The influence of viscosity is also seen in the slight increase of the Arrhenius activation energy E_a with increasing $[SiO_2]/[Al_2O_3]$ ratio. The biggest compositional influence is nevertheless found with the $[Al_2O_3]/[Ln_2O_3]$ ratio which decrease increases E_a and hence highest E_a are found for the less polymerized compositions containing the smallest amount of Al_V species. This is consistent with a localization of Ln^{3+} ions nearby Al_{IV} species already suggested by the $\overline{C}_Q^{IV} > \overline{C}_Q^{V}$ measured on glasses, the close presence of such a big cation hindering the vibrations of the aluminum tetrahedron.

As the $[Al_2O_3]/[SiO_2]$ ratio increases, we expect to reach the regime observed for aluminates and aluminosilicates melts containing less than 50 mol% of SiO_2 for which the aluminum speciation is directly correlated to the shear viscosity. There might therefore exist an

$[Al_2O_3]/[SiO_2]$ threshold above which the local aluminum thermal vibrations are directly correlated to the macroscopic viscous flow, leading to the shorter correlation times experimentally observed.

Conclusions

This investigation of a series of yttrium– and lanthanum–aluminosilicates glasses and melts led us to describe the evolution of the five–fold coordinated aluminum's population as a function of composition. In these glasses, a quantitative simulation of the high–field high–speed MAS ^{27}Al spectra showed that up to 20% of Al_V is found, predominantly in the peraluminous $[Al_2O_3]/[Ln_2O_3]>3$ region where the charge compensation of Al_{IV} is not achieved by Ln^{3+}. This concentration does not evolve markedly in this region suggesting that a mechanism such as the presence of triclusters or the increase of the Ln^{3+} coordination state stabilizes Al_{IV} units. As previously observed with alkali– and alkaline earth–aluminosilicates a significant amount (i.e. ~ 18%) of Al_V species is found at the tectosilicate composition and decreases rapidly below the tectosilicate $[Al_2O_3]/[Ln_2O_3]=3$ limit. For all compositions, the simulation of the MAS as well as the MQMAS experiments led to average quadrupolar coupling constant systematically higher for Al_{IV} than for Al_V strongly suggesting that Ln^{3+} ions are preferentially localized nearby Al_{IV} units. In agreement with their respective field–strength, yttrium–based compositions contain more Al_V than their lanthanum– counterpart.

This is also true in the high–temperature liquid state for which higher concentration of Al_V is found than in the glasses. On the other hand the aluminum average coordination state is found to decrease as a function of $[Al_2O_3]/[Ln_2O_3]$ as well as a function of the temperature, suggesting that the mechanism(s) stabilizing Al_{IV} units in the peraluminous region is (are) favored at low concentration of modifiers and low temperature. Ln_2O_3 is found to play a modifier role, with lanthanum–containing compositions being more "fragile" than yttrium–ones. From correlation times evaluated from line-width measurements, we showed that the motions responsible for the NMR relaxation of aluminum are not correlated with the movements responsible for the macroscopic shear viscosity, in contrast with aluminate compositions. This is a clear sign of a decoupling between the bond breaking and the vibration time scales for those compositions and in the temperature range explored. The evolution as a function of composition of the activation energies of the vibrations driving the ^{27}Al NMR relaxation also s that the presence of Ln^{3+} cations is favored nearby Al_{IV} compared to Al_V species.

Further works are in progress on those glasses, aiming primarily at two goals. (1) Double–resonance experiments along with ^{17}O enrichments have been started to better describe

the connectivity in those systems and help addressing the question of the presence of tri-clusters and the quantification of non-bridging oxygens. (2) The implementation on the 17.6 T spectrometer of the ^{27}Al high–temperature time–resolved NMR experimental setup is in progress to take advantage of the increased sensitivity at high field and hopefully observe the liquid state closer to the glass transition temperature.

Acknowledgements

PF is grateful to Professor Noritaka Saito for providing the high–temperature viscosity data of reference 48 and to Dr D. Neuville for helpful discussions. NS is very grateful for the French Education Minister to be able to continue research on these glasses. Financial support of the GdR “Nomade” (New Materials for Nuclear Waste) is greatly acknowledged as well as the region Centre which provided funds for the purchase of the 750 MHz WB equipment.

References

1 Kohli, J.T.; Shelby, J.E.; *Phys. Chem. Glass.* **1991**, *32*, 67

2 Shelby, J. E.; Minton, S. M.; Lord C. E.; Tuzzolo M. R. *Phys. Chem. Glass.* **1992**, *33*, 93

3 Kohli, J. T.; Condrate, R. A.; Shelby, Snr; Shelby, J.E. *Phys. Chem. Glass.* **1993**, *34(3)*, 81-87

4 Aronne, A.; Esposito, S.; Pernice, P. *Mater. Chem. Phys.* **1997**, *51*, 163-168

5 Hyatt, M. J.; Day, D. E. *J. Am. Ceram. Soc.* **1987**, *70*, C283

6 Kohli, J. T.; Shelby, J. E. *J. Am. Ceram. Soc.*, **1991**, *74*, 1031

7 Makishima, A.; Tamura, Y.; Sakaino, T. *J. Am.Ceram. Soc.* **1978**, *61*, 247

8 Setsuhisa, T.; Kazuyuki, H.; Naohiro Soga, S. *J. Am. Ceram. Soc.* **1992**, *73*, 503

9 Johnson, J.; Weber, R.; Grimsditch, M. *J. Non Cryst. Sol.* **2005**, *351*, 650

10 Nogami, N.; Hayakawa, H.; Sugioka, N.; Abe, Y. *J. Am. Ceram. Soc.*, **1996**, *79*, 1257

11 Nogami, M.; Abe, Y. *J. Appl. Phys.* **1997**, *81*, 6351

12 Leturcq, G.; Berger, G.; Advocat, T.; Vernaz, E. *Chem. Geol.* **1999**, *160*, 39

13 Bois, L.; Guittet, M. J.; Barré, N.; Trocellier, P.; Guillopé, S.; Gautier, M.; Verdier, P.; Laurent, Y. *J. Non Cryst. Sol.* **2000**, *276*, 181

14 Bois, L.; Barré, N.; Guittet, M. J.; Guillopé, S.; Trocellier, P.; Gautier, M.; Verdier, P.; Laurent, Y. *J. Non Cryst. Sol.* **2002**, *300*, 141

15 Mazza, D.; Ronchetti, S.; *Mat. Res. Bul.* **1999**, *34*, 1375

16 Vomaka, P.; Babushkin, O. *J. Eur. Ceram. Soc.* **1995**, *15*, 921

17 Kolitsch, U. *Ph. D. Thesis*, Univ. Stuttgard, 1995

18 Fabrichnaya, O.; Seifert, H. J.; Weiland, R.; Ludwig, T.; Aldinger, F.; Navrotsky, A. *Z. Metallkd.* **2001**, *92*, 1083

19 Toropov, N. A.; Bondar, I. A. *Izv. Akad. Nauk. SSSR Otd Khim. Nauk.* **1961**, 547

20 Kolitsch, U.; Seifert, H. J.; Ludwig, T.; Aldinger, F. *J. Mater; Res.* **1999**, *14*, 447

21 Sadiki, N.; Coutures, J.P.; Fillet, C.; Dussossoy, J.L. *J. Nucl. Mat.* **2006**, *348*, 70

22 Zhang, Y.; Navrotsky, A. *J. Am. Ceram. Soc.* **2003**, *86(10)*, 1727-1732

23 Zhang, Y.; Navrotsky, A. *J. Non Cryst. Solids* **2004**, *341*, 141-151

24 Hwa, L.G.; Lee, T.H., Szu, S.P. *Mat. Res. Bull.* **2003**, *39*, 33-40

25 Shelby, J.E.; Kohli, J.T. *J. Am. Ceram. Soc.* **1990**, *73(1)*, 39-42

26 Schaller, T. Stebbins, J. F. *J. Phys. Chem.* **1998**, *102*, 10690-10697

27 Kohli, J. T.; Shelby, J. E.; Frye, J. S. *Phys. Chem. Glasses* **1992**, *33(3)*, 73-78

28 Clayden, N. J.; Esposito, S.; Aronne, A.; Pernice, P. *J. Non Cryst. Solids* **1999**, *258*, 11-19

29 Sen, S.; Youngman R. E. *J. Phys. Chem. B* **2004**, *108*, 7557-7564

30 Marchi, J.; Morais, D. S.; Schneider J.; Bressiani, J. C.; Bressiani, A. H. A. *J. Non Cryst. Solids* **2005**, *351*, 863-868

31 Massiot, D.; Touzo, B.; Trumeau, D.; Coutures, J.-P.; Virlet, J.; Florian, P.; Grandinetti, P.J. *Solid. State Nuc. Magn. Reson.* **1996**, *6(1)*, 73-83

32 Massiot, D. *J. Magn. Reson. A* **1996**, 122, 240-244

33 Florian, P.; Massiot, D.; Poe, B.; Farnan, I.; Coutures, J.-P. *Solid State NMR* **1995**, *5*, 233-238

34 Massiot, D.; Trumeau, D.; Touzo, B.; Farnan, I.; Rifflet, J.-C.; Douy, A.; Coutures, J.-P. *J. Phys. Chem.* **1995**, *99*, 16455-16459

35 Massiot, D.; Fayon, F.; Capron, M.; King, I.; Le Calvé, S.; Alonso, B.; Durand, J.-O.; Bujoli, B.; Gan, Z.; Hoatson, G. *Magn. Reson. Chem.* **2002**, *40*, 70-76

36 Czjzek, G.; Fink, J.; Götz, F.; Schmidt, H.; Coey, J. M. D.; Rebouillat, J. P.; Lienard, A. *Phys. Rev. B* **1981,** *23*, 2513

37 Le Caër, G.; Brand, R. A. *Phys. Condens. Matter* **1998**, *10*, 10715-10774

38 Neuville, D. R.; Cormier, L. ; Massiot, D. *Geochim. Cosmochim. Acta* **2004**, *68*, 5071-5079

39 Gruener, G.; Odier, P.; De Souza Meneses, D.; Florian, P.; Richet, P. *Phys. Rev. B* **2001**, *64*, 024206

40 Capron, M.; Florian, P.; Fayon, F.; Trumeau, D.; Hennet, L.; Gaihlanou, M.; Thiaudière, D.; Landron, C.; Douy, A.; Massiot, D. *J. Non Cryst. Solids* **2001**, *293-295*, 496-501

41 Coutures, J. P.; Rifflet, J. C.; Florian, P.; Massiot, D. Rev. Int. Hautes Tempér. Réfract. **1994**, *29(4)*, 1-20

42 Capron, M. *Ph. D. Thesis*, Univ. Orléans, 2001

43 Poe, B. T.; McMillan, P. F.; Coté, B.; Massiot, D.; Coutures J.-P. *J. Phys. Chem.* **1992**, *96*, 8220-8224

44 Whittaker, E. J. W.; Muntus, R. *Geochim. Cosmochim. Acta* **1970**, *34*, 945-956

45 Abragam, A. *Principles of Nuclear Magnetism*, Clarendon Press, Oxford, 1961

46 Petit, D.; Korb, J.-P. *Phys. Rev. B* **1988**, *37(10)*, 5761-5780

47 Bloembergen, N.; Purcell, E. M.; Pound, R. V. *Phys. Rev.* **1948**, *73*, 679

48 Saito, N.; Kai, K.; Furusho, S.; Nakashima, K.; Mori, K. *J. Am. Ceram. Soc.* **2003**, *86(4)*, 711-716

49 Dingwell, D.B.; Webb, S.L. *Eur. J. Mineral.* **1990**, *2*, 427-449

50 Risbud, S. H.; Kirkpatrick, R. J.; Taglialvore, A. P.; Montez, B. *J. Am. Ceram. Soc.* **1987**, *70(1)*, C10-C12

51 Sato, R. K.; McMillan, P. F.; Dennison, P.; Dupree, R. *J. Phys. Chem.* **1991**, *95*, 4483-4489

52 Toplis, M. J.; Dingwell, D. B.; Lenci, T. *Geochim. Cosmochim. Acta* **1997**, *61(13)*, 2605-2612

53 Stebbins J. F.; Xu, Z. *Nature* **1997**, *390*, 60-62

54 Iuga, D.; Morais, C.; Gan, Z.; Neuville, D. R.; Cormier, L.; Massiot, D. *J. Am. Chem. Soc.* **2005**, *127*, 11540-11541

55 Stebbins, J. F.; Farnan I. *Science* **1992**, *255*, 586-589

56 Stebbins, J. F.; Kroeker, S.; Lee, S. K.; Kiczenski, T. J. *J. Non Cryst. Solids* **2000**, *275*, 1-6

57 Neuville, D. R.; Cormier, L.; Massiot, D. *Chem. Geol.* **2006**, *229*, 173-185

58 Toplis, M. J.; Kohn, S. C., Smith, M. E.; Poplett, I. J.F. *Am. Miner.* **2000**, *85*, 1556-1560

59 Angell, C. A. *J. Non-Cryst. Solids* **1988**, *102*, 205-221

60 Angell, C. A. *J. Non-Cryst. Solids* **1991**, *131-133*, 13-31

61 Bondar, I. A.; Galakhov, F. Ya.; *Bull. Acad. Sci. USSR, Div. Chem. Sci.* **1964**, *7*, 1231-1232

Table captions

Table 1: Theoretical and experimental compositions of the glasses investigated.

Table 2: Results of the ^{27}Al 1D MAS and 2D MQMAS simulations for all compositions investigated.

Table 3: Results derived from the high–temperature experiments along with some literature data.

Sample	Starting weight%			Starting mol%			Measured mol%			Al/Si	Al/Ln	T_g (°C)	T_c (°C)	T_m (°C)
	Y_2O_3	Al_2O_3	SiO_2	Y_2O_3	Al_2O_3	SiO_2	Y_2O_3	Al_2O_3	SiO_2					
Y04A14	10	20	70	3.15	13.95	82.89	3.80	13.7	82.5	0.166	3.61	913	1132	1341
Y04A22	10	25	65	3.23	17.88	78.89	3.58	21.9	74.5	0.294	6.12	917	1101	1341
Y04A21	10	30	60	3.31	22.00	74.69	4.29	20.9	74.8	0.279	4.86	914	1087	1338
Y12A13	30	15	55	11.11	12.31	76.58	12.1	13.1	74.9	0.175	1.09	916	1150	1360
Y12A17	30	20	50	11.43	16.89	71.67	11.4	16.9	71.7	0.236	1.49	913	1142	1358
Y12A20	30	25	45	11.78	21.75	66.47	12.4	20.4	67.1	0.304	1.64	914	1202	1358 1378
Y12A27	30	30	40	12.15	26.92	60.93	11.8	26.7	61.6	0.434	2.27	912	1165 1208	1335 1367
Y08A23	20	30	50	7.28	24.21	68.50	8.04	23.1	68.8	0.336	2.88	906	1212	1344
Y05A22	15	30	55	5.20	23.06	71.74	4.45	22.4	73.1	0.307	5.04	917	1155	1347
	La_2O_3	Al_2O_3	SiO_2	La_2O_3	Al_2O_3	SiO_2	La_2O_3	Al_2O_3	SiO_2					
L02A17	10	20	70	2.20	14.10	83.70	2.69	16.9	80.4	0.211	6.29	899	1123	1454
L02A19	10	25	65	2.25	18.04	79.62	2.17	18.6	79.2	0.235	8.59	900	1100	
L02A23	10	30	60	2.32	22.23	75.45	1.91	23.5	74.6	0.314	12.3	910	1055	
L08A13	30	15	55	7.98	12.74	79.28	8.01	12.7	79.3	0.161	1.59	874		
L08A16	30	20	50	8.22	17.50	74.29	8.31	15.4	76.3	0.202	1.86	884		
L08A22	30	25	45	8.47	22.56	68.98	8.45	22.3	69.3	0.322	2.64	886	1194	
L08A28	30	30	40	8.74	27.93	63.33	9.18	28.4	62.4	0.456	3.10	892	1098	
L05A24	20	30	50	5.17	24.77	70.06	5.11	24.1	70.8	0.340	4.71	902	1104	
L04A24	15	30	55	3.66	23.40	72.86	3.76	23.9	72.4	0.330	6.36	903	1130	

Table 1

Sample		% Al_{IV}	% Al_{V}	% Al_{VI}	$\overline{\delta}_{iso}^{IV}$ (ppm)	$\overline{\delta}_{iso}^{V}$ (ppm)	$\overline{\delta}_{iso}^{VI}$ (ppm)	$\overline{C}_{Q}^{IV}$ (MHz)	$\overline{C}_{Q}^{V}$ (MHz)	$\sigma(\delta_{iso}^{IV})$ (ppm)	$\sigma(\delta_{iso}^{V})$ (ppm)
Y04A14	1D	80.8	16.6	2.7	64.0	36.6	11.2	10.7		17.3	
	2D	78.5	21.4	-	62.6	34.9	-	9.00	7.30	15.6	15.8
Y04A22	1D	79.0	18.0	3.0	64.2	36.7	11.4	11.4		16.8	
	2D	76.6	23.4	-	62.6	35.2	-	9.06	7.31	16.0	15.1
Y04A21	1D	73.3	22.4	4.3	64.8	37.4	11.4	10.9		17.6	
	2D	76.2	23.9	1.4	62.9	35.3	-	9.35	7.16	16.2	14.7
Y12A13	1D	92.3	5.9	1.8	63.7	32.9	10.2	10.1		18.2	
	2D	89.6	10.4	-	60.3	32.2	-	7.80	6.80	19.8	*20.0*
Y12A17	1D	90.1	8.6	1.4	63.8	34.9	7.4	10.2		14.3	
	2D	89.9	10.1	-	62.3	34.7	-	8.31	6.13	15.1	17.1
Y12A20	1D	87.8	10.6	1.6	64.2	36.1	9.2	10.1		16.1	
	2D	85.2	14.8	-	62.3	33.4	-	8.67	7.38	15.1	16.2
Y12A27	1D	82.1	15.1	2.8	65.4	36.8	9.7	9.86		16.1	
	2D	81.2	18.8	-	63.9	34.9	-	8.45	7.32	15.4	15.7
Y08A23	1D	85.7	12.0	2.3	63.9	35.4	9.3	10.6		19.7	
	2D	84.7	15.3	-	61.4	35.3	-	8.32	6.73	18.2	*15.0*
Y05A22	1D	82.3	15.8	1.9	64.1	36.5	9.6	11.0		17.2	
	2D	81.0	19.0	-	62.6	35.2	-	9.03	7.29	15.6	15.6
L02A17	1D	85.1	12.4	2.5	61.9	35.4	11.5	11.1		17.1	
	2D	83.9	16.1	-	60.7	34.7	-	9.47	7.36	14.8	16.1
L02A19	1D	80.2	17.1	2.7	63.4	36.7	10.9	11.2		17.0	
	2D	79.1	20.9	-	61.6	34.4	-	9.23	7.15	15.5	16.1
L02A23	1D	75.6	20.5	3.9	63.7	37.0	12.0	10.9		18.0	
	2D	81.0	19.0	-	61.5	34.4		8.96	7.28	15.1	16.0
L08A13	1D	100.0	-	-	62.2	-	-	9.26		13.7	
	2D	94.6	5.4	-	61.1	34.2	-	7.93	7.08	13.6	*14.0*
L08A16	1D	94.2	5.0	0.8	62.9	34.4	4.5	8.91		16.3	
	2D	92.2	7.8	-	61.2	33.6	-	8.00	7.08	14.2	*14.0*
L08A22	1D	85.2	13.2	1.7	63.1	37.0	9.7	8.53		16.5	
	2D	88.5	11.5	-	62.2	34.9	-	8.04	7.34	14.0	
L08A28	1D	81.6	15.9	2.6	64.1	37.2	9.7	8.58		16.6	
	2D	86.6	13.4	-	63.2	34.7	-	8.11	7.12	14.6	15.9
L05A24	1D	78.2	18.6	3.2	62.6	36.5	11.3	9.12		18.0	
	2D	84.1	15.9	-	61.6	35.1	-	8.69	6.92	14.9	17.1
L04A24	1D	81.1	16.5	2.4	63.1	36.1	10.4	10.4		17.4	
	2D	81.0	19.0	-	61.6	34.5	-	8.87	7.28	15.2	15.7

Table 2

Sample	Al/Ln	Si/Al	T (°C)	δ (ppm)	$\Delta\nu_{1/2}$ (Hz)	τ_c (ps)	$\Delta\delta/\Delta T$ (10^3ppm/°C)	$\delta_{1900°C}$ (ppm)	E_a (kJ/mol)	Ref.
Y04A22	6.12	3.4	2177	56.2	598	19.8	0.6	56.4	39.8	
Y04A21	4.86	3.59	1985	55.6	588	19.5	3.0	55.2	46.9	
Y08A23	2.88	2.97	1895	55.9	467	15.5	-0.3	55.7	60.1	
Y12A13	1.09	5.72	2066	57.6	478	15.9	-1.3	57.8	73.3	
Y12A17	1.49	4.24	2067	57.4	466	15.4	-1.2	57.0	61.3	
L02A23	12.3	3.18	2017	56.1	556	18.4	1.5	55.5	55.4	
L05A24	4.71	2.94	2089	56.7	269	8.91	-0.7	56.6	88.4	
L08A13	1.59	6.23	2192	57.4	338	11.2	-2.5	58.0	96.2	
L08A16	1.86	4.95	2138	59.5	398	13.2	-2.8	58.8	129	
Al_2O_3	-	-	2396	58.7	112	3.70	5.2	57.3	83.4	
#4 : Y14A20	1.38	3.38							289	48
#5 : Y17A19	1.11	3.39							302	
#6 : Y20A18	0.90	3.41							305	
$CaAl_2Si_2O_8$	1.00	4.00							187	42
$CaAl_2O_4$	1.00	-					-6.0		142	34

Table 3

Figure captions

Figure 1: Ln_2O_3–Al_2O_3–SiO_2 ternary system with glass compositions used in this study. Open symbols : Ln=Y, filled symbols : Ln=La. Liquidus lines are taken from the Y_2O_3–Al_2O_3–SiO_2 phase diagram[61].

Figure 2: Stack plot of the ^{27}Al MAS NMR spectra for all yttria (up) and lanthana-based (down) compositions.

Figure 3: Simulations of the ^{27}Al 1D MAS and 2D MQMAS spectra for the $4Y_2O_3$–$21Al_2O_3$–$74SiO_2$ (top) and $2La_2O_3$–$23Al_2O_3$–$75SiO_2$ (bottom) compositions. The dashed lines corresponds to the experimental spectra obtained at 9.4 T. Simulations take into account central <-1/2,1/2> transition and their related spinning sidebands of the external <±1/2, ±3/2> transitions.

Figure 4: Evolution of the proportions of Al_{IV} and Al_V species as a function of the molar ratios $[Al_2O_3]/[Ln_2O_3]$ (top) and the molar content $[SiO_2]$ (bottom). Filled symbols: LAS glasses, opened symbols: YAS glasses, line labels: $[Ln_2O_3]$ (mol%). Lines are guide for the eyes only emphasizing the evolution at fixed $[Ln_2O_3]$ content.

Figure 5: Representative high–temperature spectra obtained in the liquid state with one scan at the beginning of the free cooling.

Figure 6: Evolution of the line position in the high–temperature liquid phase as a function of temperature and for a set of selected compositions. Triangles up: Y04A22 and L02A19, circles: Y04A21 and L02A23, diamonds: Y08A23 and L05A24, squares: Y12A13 and L08A13, triangles down: Y12A17 and L08A16, crosses: Al_2O_3 (Ln = Y or La). Similar filled symbols correspond to the related average isotropic chemical shifts obtained from the room–temperature experiments (see text). Lines are linear fit through the high temperature data.

Figure 7: Evolution of the chemical shift slope $\Delta\delta/\Delta T$ (squares, bottom, left scale) and position δ at 1900°C (triangles, top, right scale) in the high–temperature liquids as a function of the $[Al_2O_3]/[Ln_2O_3]$ molar ratio. Open symbols are for YAS compositions and filled symbols for LAS ones. Lines are linear fit through the high temperature data.

Figure 8: Evolution of the logarithm of the correlation time τ_c derived from the high–temperature NMR linewidth as a function of 1000/T for : Y04A22 and L02A19 (triangles up), Y04A21 and L02A23 (circles), Y08A23 and L05A24 (diamonds), Y12A13 and L08A13 (squares), Y12A17 and L08A16 (triangles down), Al_2O_3 (crosses) with Ln = Y or La. Filled symbols are derived from high–temperature viscosity measurements taken from reference 48:

Y14A20 (circles), Y17A19 (triangles) and Y20A18 (squares). Lines are linear fit through the data.

Figure 9: Arrhenius activation energies calculated from the linear fits displayed in figure 8. Symbols for NMR experiments: open squares are for YAS compositions, filled triangles for LAS, open circle for $CaAl_2Si_2O_8$ (ref. 42) and open diamond for $CaAl_2O_4$ (ref. 34). Filled squares are obtained from viscosity measurements (ref. 48). Lines are linear fit through the high temperature data and symbol labels are the $[SiO_2]/ [Al_2O_3]$ molar ratio.

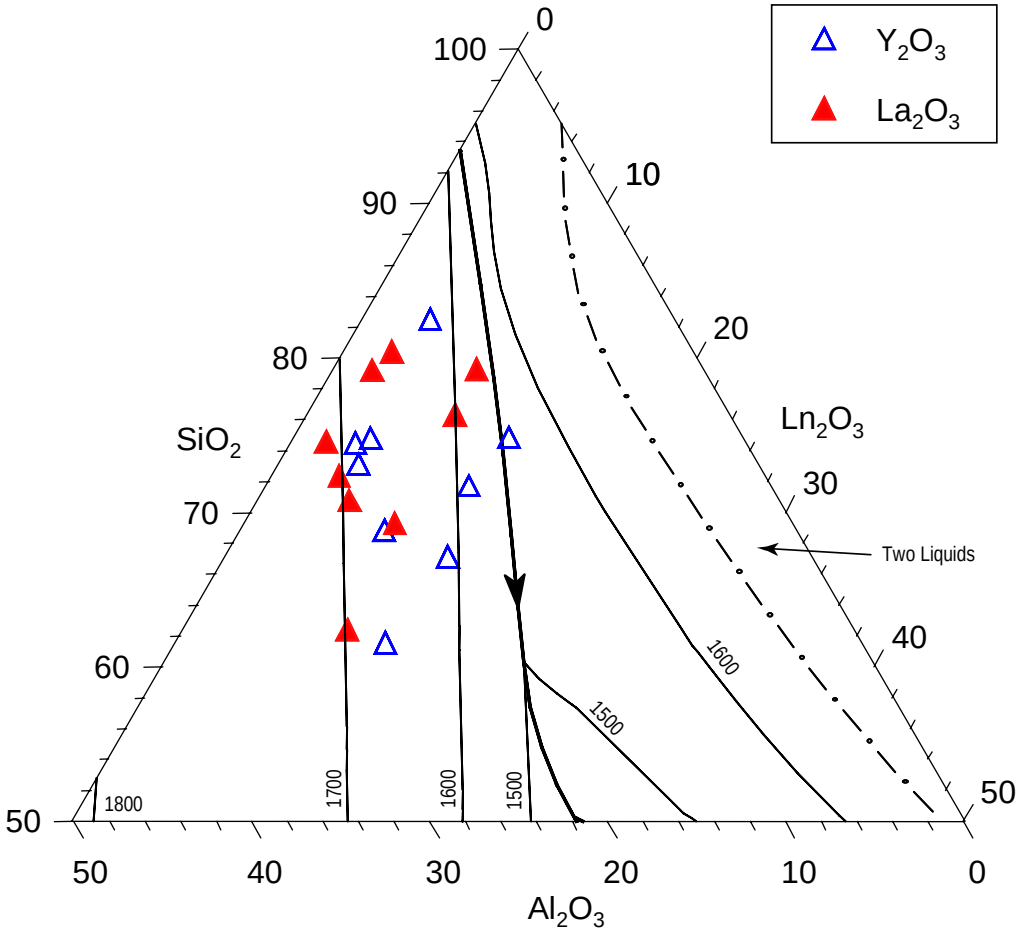
Y2O3
La2O3
SiO2
Ln2O3
Al2O3
Two Liquids
1800
1700
1600
1500
1600
1500
0
100
10
90
20
80
30
70
40
60
50
50
50
40
30
20
10
0

Figure 1

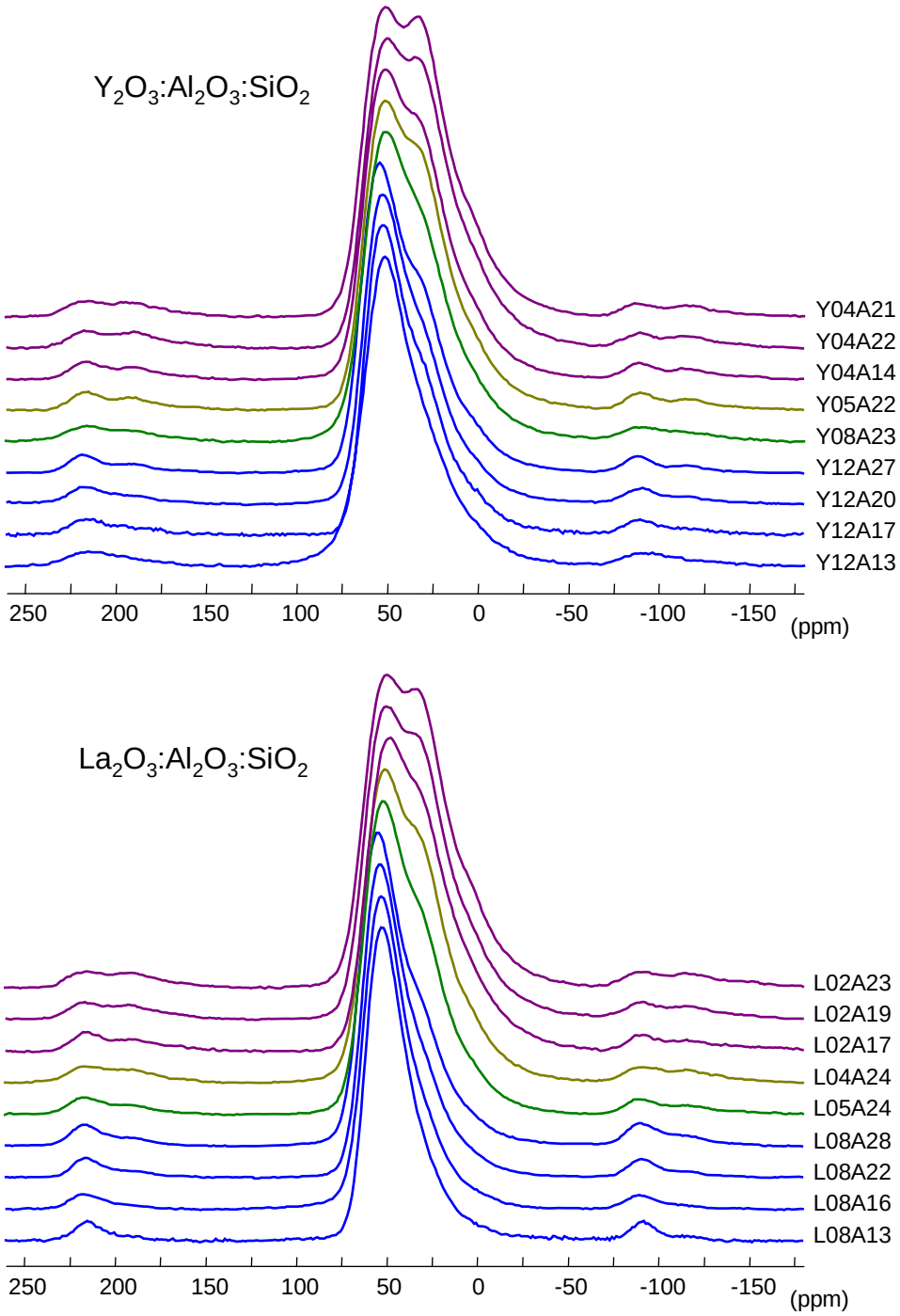
Y2O3:Al2O3:SiO2
Y04A21
Y04A22
Y04A14
Y05A22
Y08A23
Y12A27
Y12A20
Y12A17
Y12A13
250
200
150
100
50
0
-50
-100
-150
(ppm)
La2O3:Al2O3:SiO2
L02A23
L02A19
L02A17
L04A24
L05A24
L08A28
L08A22
L08A16
L08A13
250
200
150
100
50
0
-50
-100
-150
(ppm)

Figure 2

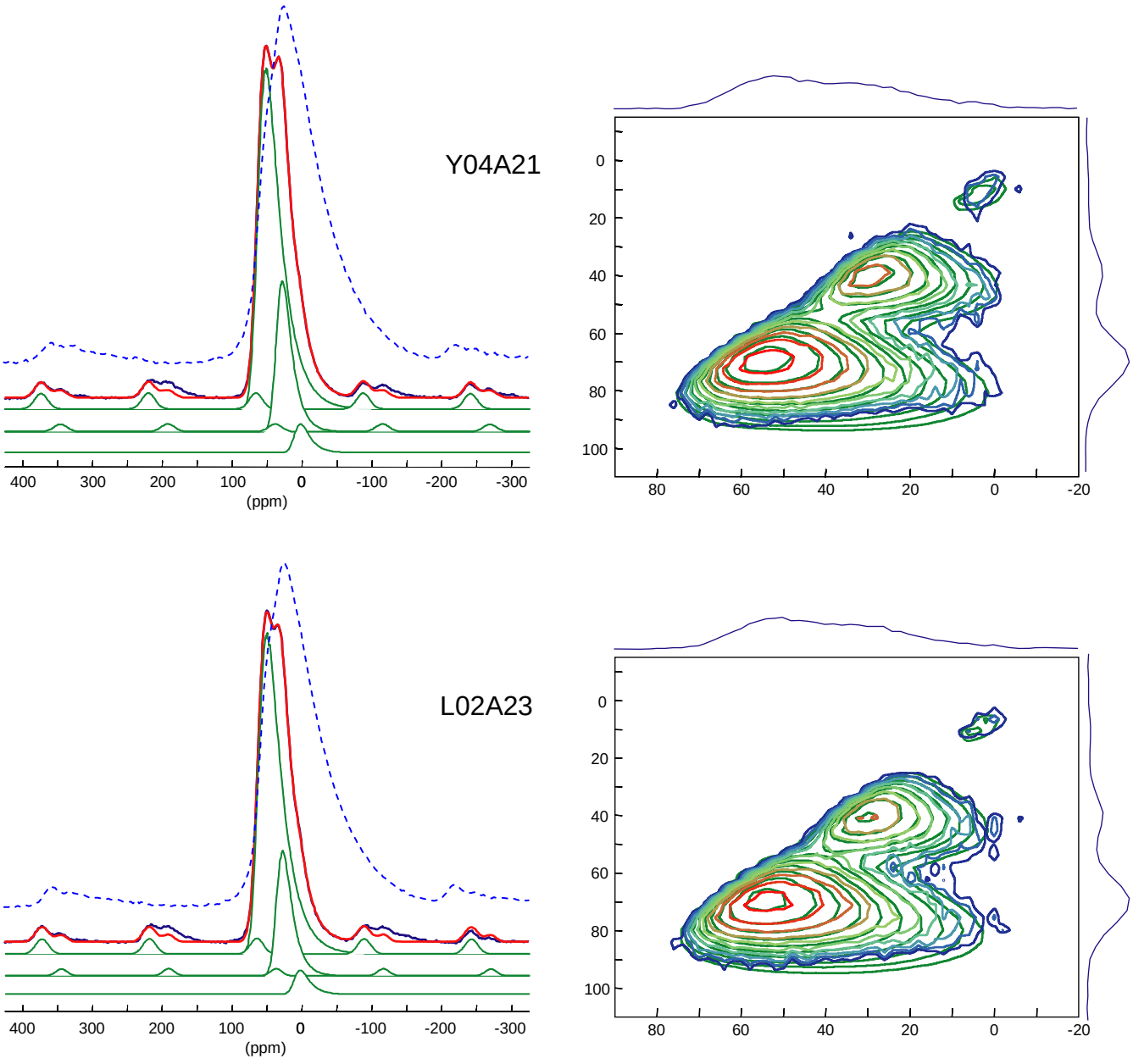
Y04A21
L02A23
400
300
200
100
0
-100
-200
-300
(ppm)
0
20
40
60
80
100
80
60
40
20
0
-20

Figure 3

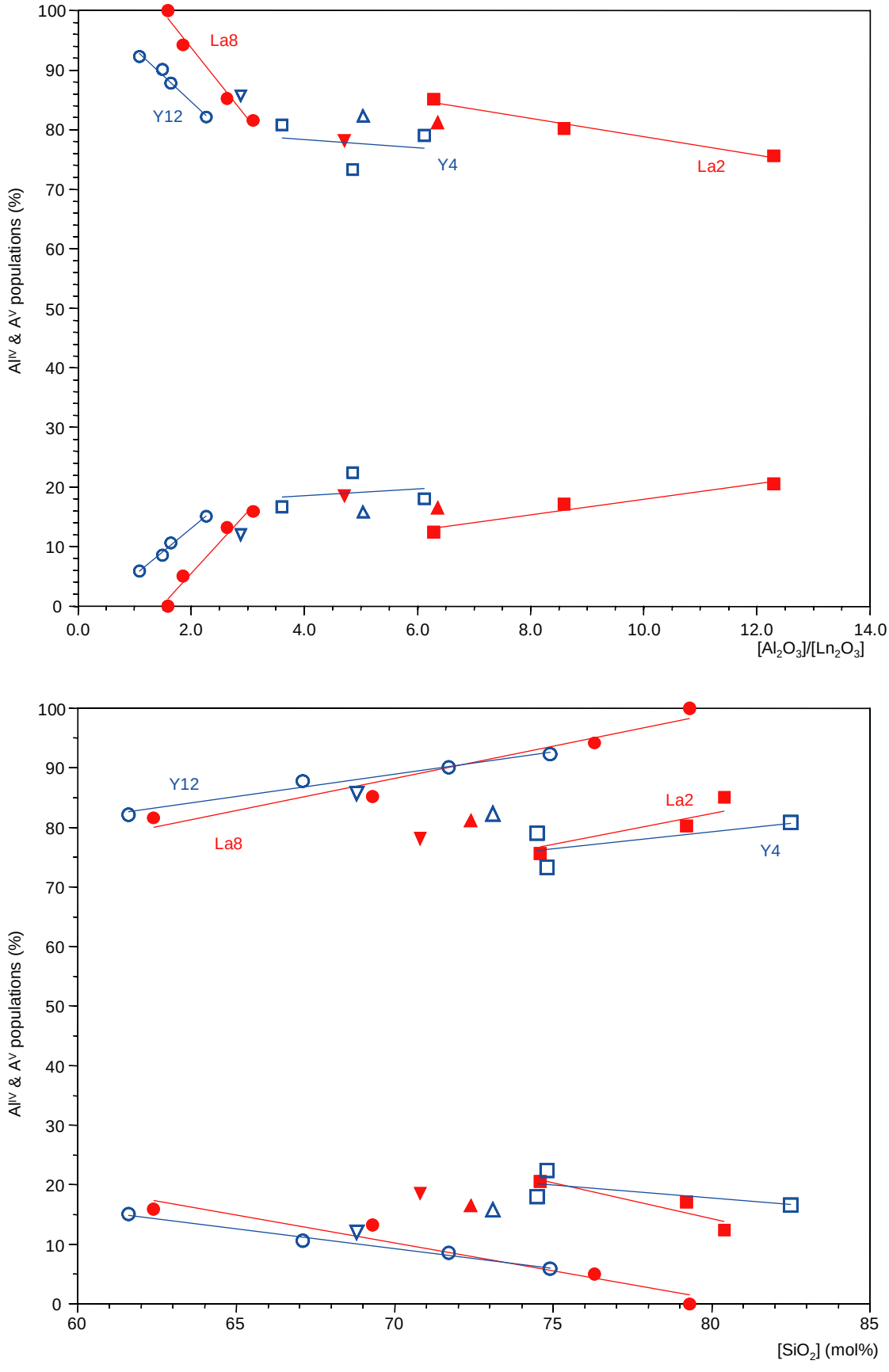
La8
Y12
Y4
La2
Al^{IV} & A^{V} populations (%)
$[Al_2O_3]/[Ln_2O_3]$
Y12
La8
La2
Y4
Al^{IV} & A^{V} populations (%)
$[SiO_2]$ (mol%)

Figure 4

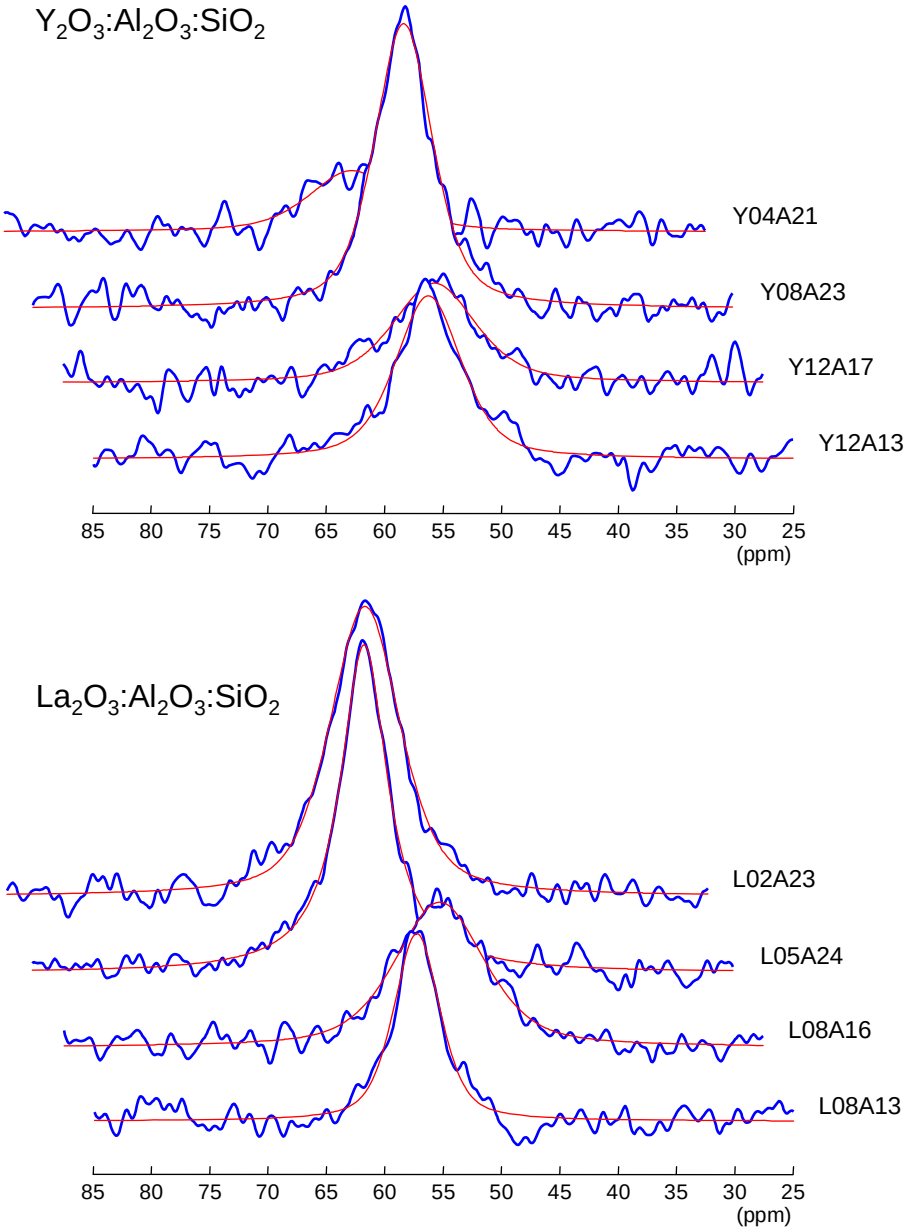
Y2O3:Al2O3:SiO2
Y04A21
Y08A23
Y12A17
Y12A13
85 80 75 70 65 60 55 50 45 40 35 30 25
(ppm)
La2O3:Al2O3:SiO2
L02A23
L05A24
L08A16
L08A13
85 80 75 70 65 60 55 50 45 40 35 30 25
(ppm)

Figure 5

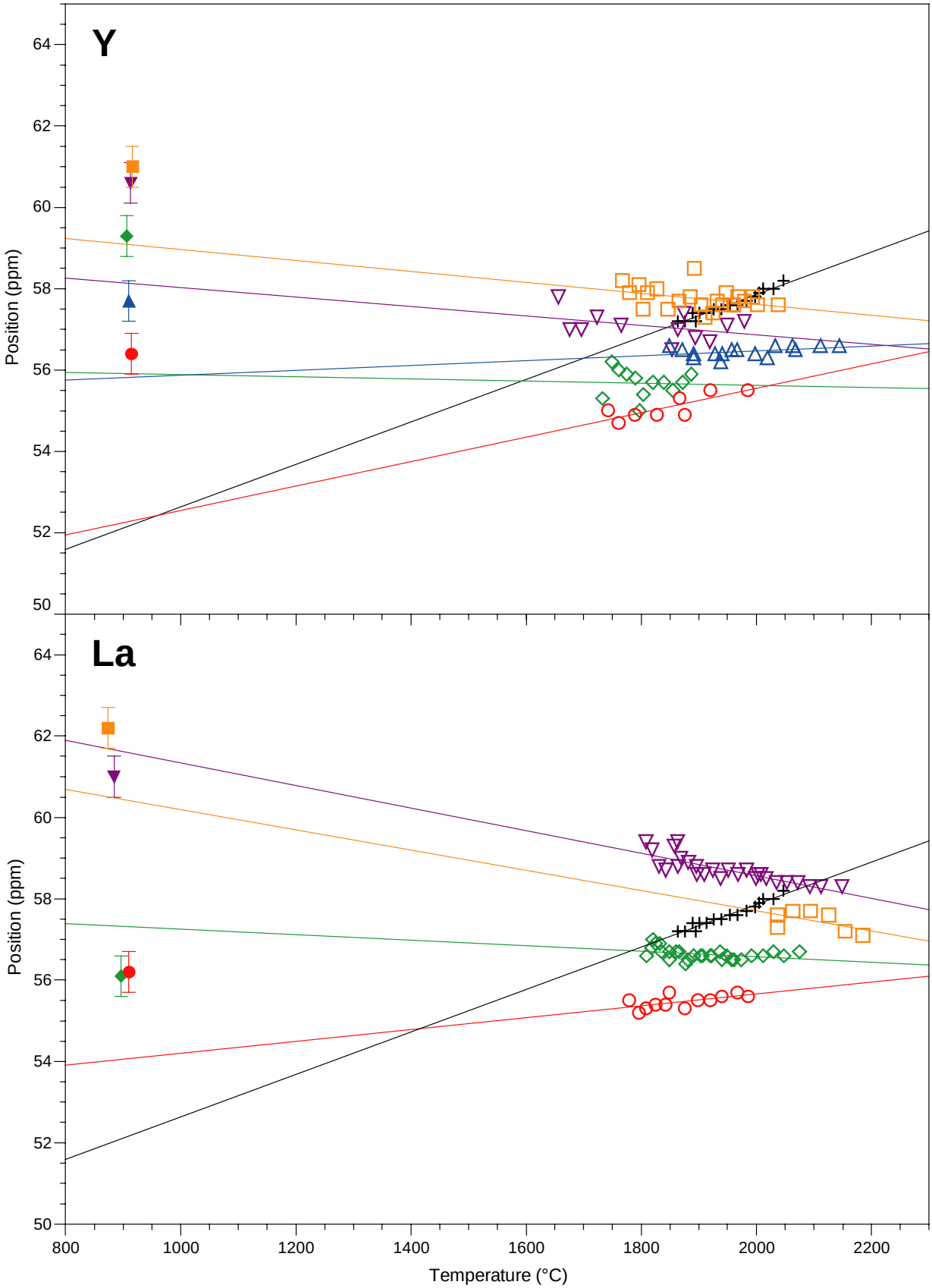
Y
La
Position (ppm)
Position (ppm)
64
62
60
58
56
54
52
50
800
1000
1200
1400
1600
1800
2000
2200
Temperature (°C)

Figure 6

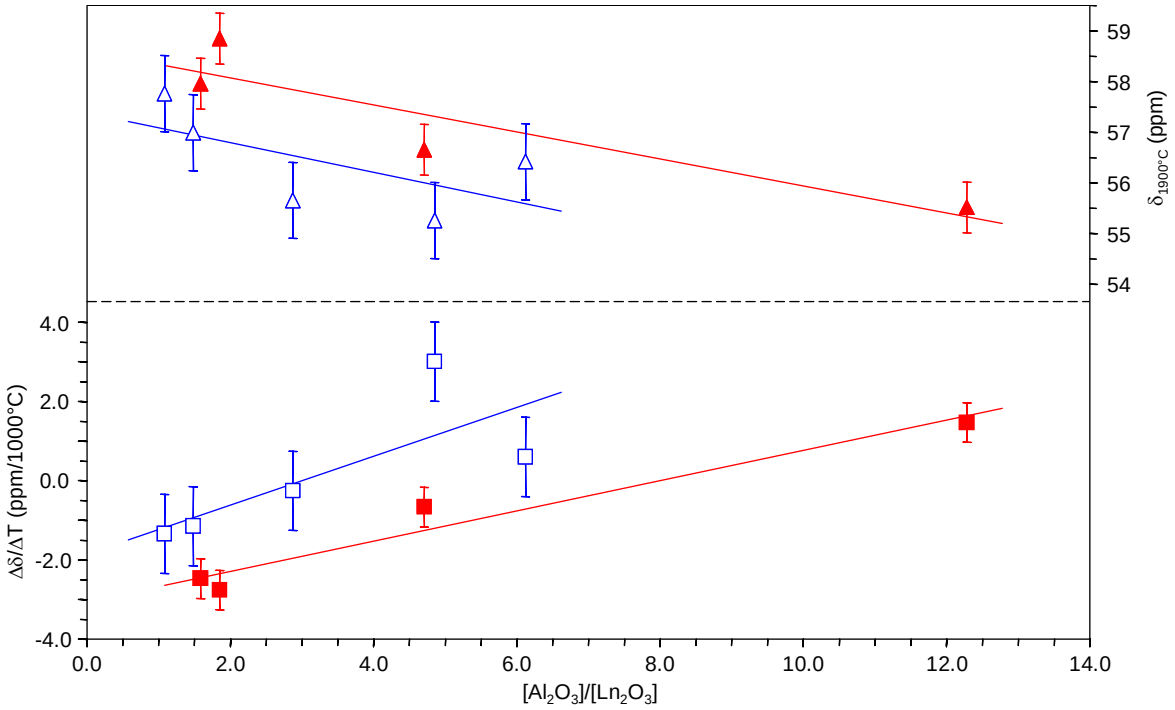
59
58
57
56
55
54
$\delta_{1900°C}$ (ppm)
4.0
2.0
0.0
-2.0
-4.0
$\Delta\delta/\Delta T$ (ppm/1000°C)
0.0
2.0
4.0
6.0
8.0
10.0
12.0
14.0
$[Al_2O_3]/[Ln_2O_3]$

Figure 7

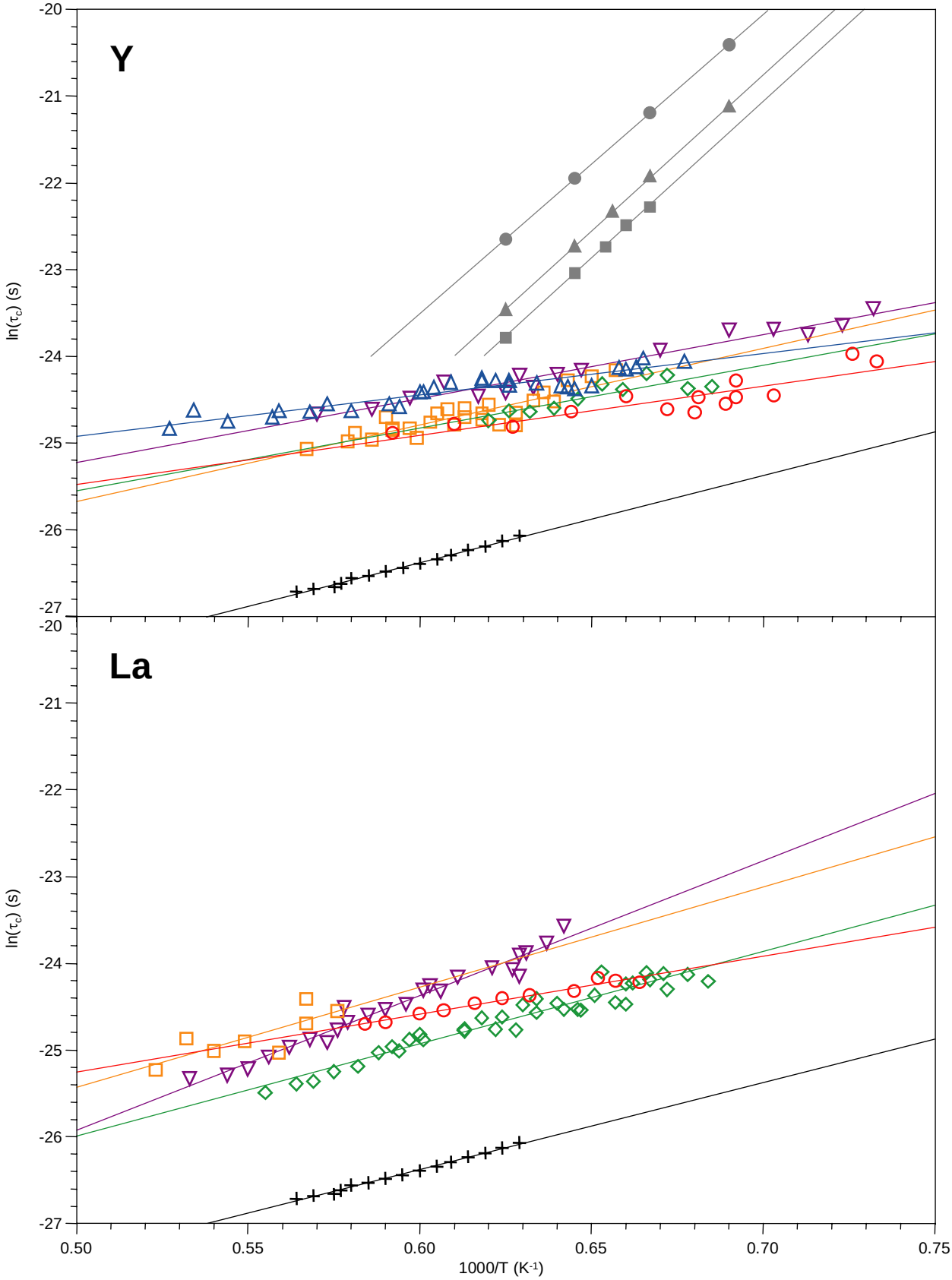

Figure 8

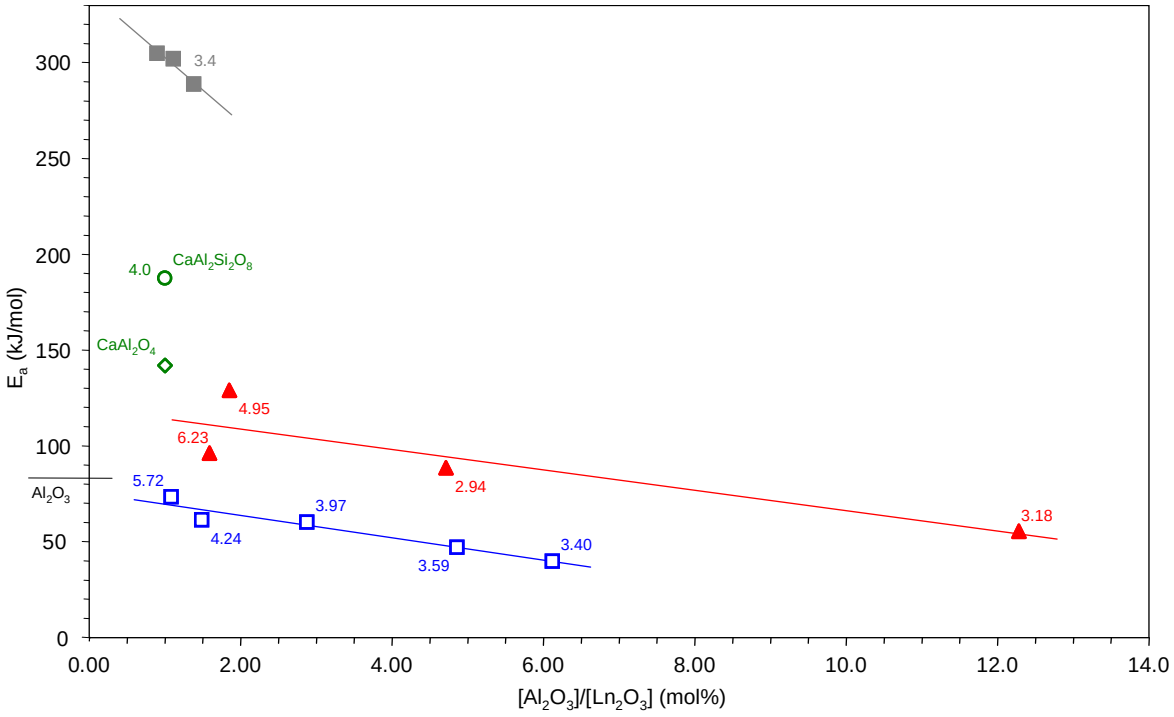
3.4
4.0
CaAl2Si2O8
CaAl2O4
4.95
6.23
2.94
3.18
5.72
3.97
4.24
3.40
3.59
Al2O3
Ea (kJ/mol)
[Al2O3]/[Ln2O3] (mol%)
0
50
100
150
200
250
300
0.00
2.00
4.00
6.00
8.00
10.0
12.0
14.0

Figure 9